J. Fluid Mech. (1983), *vol.* 129, *pp.* 283–311
Printed in Great Britain

Numerical processing of flow-visualization pictures – measurement of two-dimensional vortex flow

By KENSAKU IMAICHI AND KAZUO OHMI
Faculty of Engineering Science, Osaka University, Toyonaka, Japan

(Received 13 January 1982 and in revised form 31 October 1982)

A new system has been developed for estimating experimentally some of the principal physical variables of fluid flows, through flow-visualization and image-processing techniques. Distributions of stream function, vorticity and pressure are calculated by this system with reasonable accuracy for two examples of two-dimensional flow: namely unsteady twin-vortex flow behind a circular cylinder accelerated impulsively to constant speed, and Kármán vortices behind a circular cylinder moving at constant speed. A detailed explanation of the image-processing technique and the numerical calculation process is given first, and then some consideration is given to calculated results in these two types of flow. Comparison shows that some results of the unsteady twin-vortex experiment coincide well with those of previously published experimental investigations and theoretical calculations. Errors introduced at each stage of this system are estimated in some detail.

1. Introduction

In experimental investigations of fluid dynamics, the flow-visualization technique has the advantage of displaying the whole flow field at one time, whether steady or unsteady. In particular, when we take a picture of pathlines produced by the motion of small particles suspended in fluid, we can even estimate some quantities such as velocity and acceleration. There have been a number of examples of velocity measurement from varied flow-visualization pictures. As for two-dimensional flow past a circular cylinder, studies have been produced by Schwabe (1935), Timme (1957) and Coutanceau and Bouard (Coutanceau & Bouard 1977*a*, *b*; Bouard & Coutanceau 1980). Schwabe and Timme are concerned with analysis of the measured distribution of velocity, and, from such analysis, Schwabe obtains the pressure distribution on the cylinder surface, and Timme the circulation of shed vortices. Measurement itself is conducted rather partially or fagmentarily in their experiments. Coutanceau and Bouard have investigated in the greatest of detail the geometrical values of steady and of unsteady twin vortices, and the velocity distributions inside the vortex, though they have not analysed their measurements numerically so as to estimate other parameters of the flow. None of them, in short, has made full use of the quantitative information contained within a flow-visualization picture in order to obtain a general, systematic understanding of the flow. The reasons for this are thought to be the following: the amount of manual work required to locate the large number of particle pathlines with many types of photograph, the difficulty of numerical analysis with respect to measured velocity vectors in random arrangement, and the general assumption that accurate estimation of the results is very difficult. The present authors have therefore endeavoured to fill these gaps by determining the coordinates of particle paths both efficiently and accurately by the use of a personal computer

system with an image-processing device, and by interpolating the velocity at mesh points from among several or several tens of velocity vectors distributed around them, in order to calculate numerical distributions of stream function, vorticity and pressure. With the development of this system there arises the possibility not only of making an objective estimation of various types of flow with any initial or boundary conditions, but also of providing suggestive information for theoretical investigations, or even of producing an approximation of the first order in their analysis. In the course of a specified explanation of the image-processing technique and the numerical calculation process, an examination of the results of the two examples of two-dimensional flow mentioned above, and a detailed estimation of errors, this paper claims that the system presented here has wide application as an accurate method of evaluating fields of unsteady two-dimensional flow.

2. Experimental arrangements and numerical calculations

2.1. *Flow visualization and photography*

The flow-visualization experiments are all conducted in a towing water tank, of which a schematic illustration is given in figure 1. A quantity of aluminium powder with particles 2–7 μm in length to be used as tracers is suspended uniformly in the water of the tank after several decantations. The illumination is provided by a sheet of intense light (generated by 9 projector bulbs in linear arrangement) passing through a 5 mm wide slit. The lighting plane is situated in the midlevel horizontal cross-section of the tank. The test cylinder is fixed to the towing carriage by a rigid metal bar about 50 mm long. Two kinds of cylinders are employed here, 20 and 30 mm in diameter respectively, and both made of transparent acrylic plastic. For the purpose of photographing particle paths after regular time intervals, a 35 mm camera with an electric winding device and a Capacitance–Resistance oscillator is placed above the water tank in the position shown in figure 2. The photographic time interval available with this camera is between 1·3 and 600 s, in the case of our usual exposure time of 0·9 s. There are two possible ways of fixing the camera; one by attaching it by a metal support to the frame of the water tank, which means an observation point fixed in relation to the fluid, and the other by attaching it to the towing carriage, which means an observation point fixed in relation to the cylinder. The selection between these two depends mainly upon which is more convenient for measuring particle velocities from the resulting photographic images. When photographing the twin-vortex flow, for instance, the latter position is adopted because the resulting particle paths are long enough to be free from measurement errors. In spite of occasional adjustment of the room temperature and consequent motion of the fluid, it takes more than an hour for the particles in the tank to return to a stationary state after every disturbance (by 'stationary state' we mean that every particle is recognized as a stationary point on photographs of 1 min exposure). Negative films of 400 ASA are usually overdeveloped for better visibility. Positive images are all printed on 12×10 in. plastic-coated photographic paper of ultrahigh contrast, which expands or contracts very little. The magnification of positives is from 2·4 to 2·6, before taking optical distortion into account. According to occasional examinations made with an acceleration sensor, the motion of the towing carriage is extremely smooth and is free from mechanical vibrations of any kind, owing to the use of lubricating films attached to the rails and to the employment, in addition, of backward tension wires.

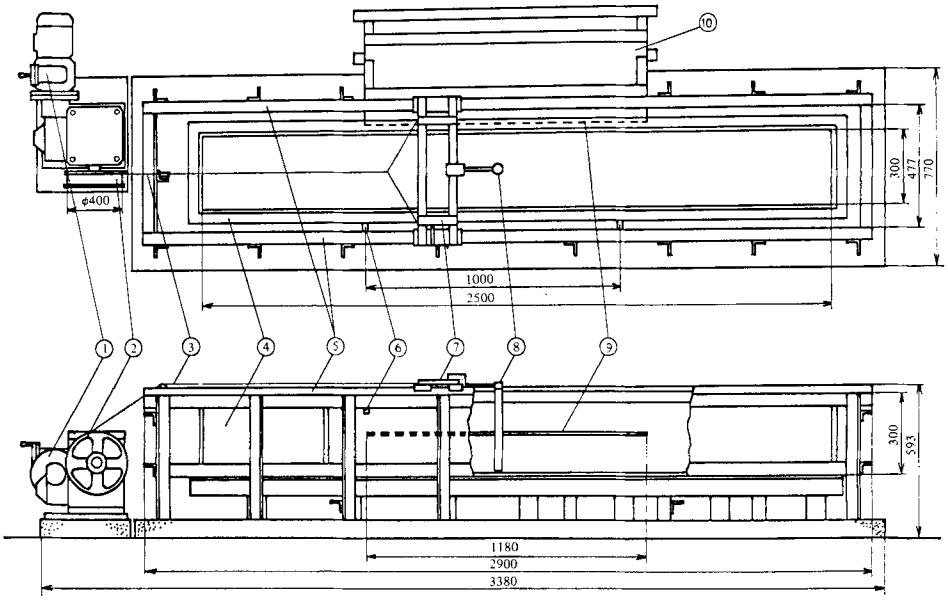

FIGURE 1. Schematic illustration of the towing water tank. 1, Variable-speed motor; 2, pulley; 3, steel wire; 4, water tank; 5, rails; 6, time-count equipment; 7, towing carriage; 8, test cylinder; 9, slit; 10, illuminator. (Unit of length: mm.)

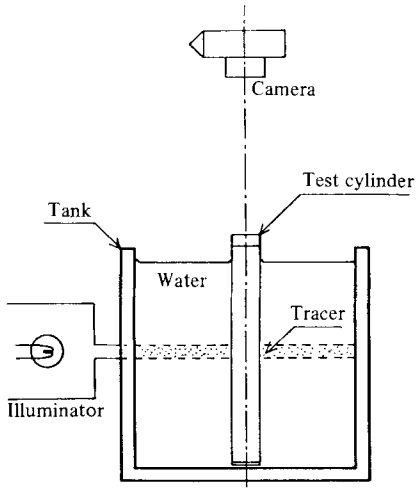

FIGURE 2. Photography of particle paths.

2.2. *Measurement of particle velocity*

Particle velocity is computed from the length of every clearly drawn particle path on the photograph and from the exposure time of the camera, so that an instantaneous velocity distribution of the flow may be obtained. The measurement of particle paths is done by the manual operation of a digitizing tablet, one of the simplest image-processing devices, which analyses x- and y-coordinates of any marked points on a photograph attached to the tablet. The two end-points of each particle path, when distinguishable, are established visually by the operator, bearing in mind the direction of flow. At the same time, output signals for the corresponding coordinates are put into the personal computer for analysis. Then the mean location of the particle

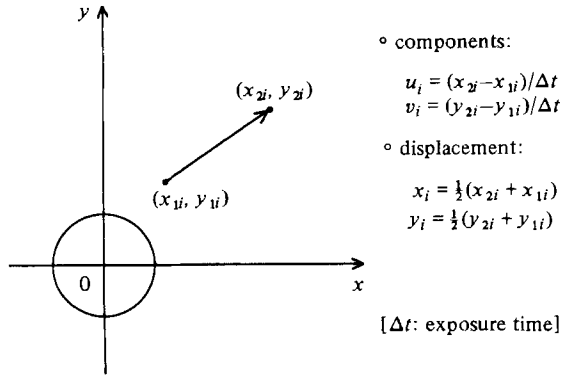

FIGURE 3. Definition of the two components of the velocity vector and of the coordinates of the mean displacement.

paths and the two components of the corresponding velocity vectors are determined by means of the computation shown in figure 3, and put into the external memory of the computer. The number of particle paths is between 2000 and 4000 per photograph, about 20 % of which are not put into the measurement because it is clear from the characteristics of their trajectories that the orientation of some of the lamellar particles has changed during the exposure time, with respect to the direction of the illumination. The time required to locate the remainder is between 2 and 4 h per photograph. The exposure time of the camera is measured electrically from the time during which the circuit between its synchronized external terminals is closed. This time measurement turns out to be accurate enough to compare with that of particle paths. As for the optical distortion introduced on the photographic images, the following corrective calibration is made with each experiment: an experimental functional formula is provided for the relationship between apparent and real distances from the centre of the photographic field, and each pair of x- and y-coordinates located on the photograph is converted into one on the real scale, thus removing all possible distortion. Figure 4 shows an example of velocity distribution as observed on the original photograph (*a*), and as image-processed and reproduced on the CRT display of the computer (*b*).

2.3. *Mesh-point velocity*

A square grid pattern is imagined as covering the entire photographic field with a view to numerical calculations, and the velocity at each of the mesh points is interpolated from among a number of neighbouring velocity vectors. Supposing two linear equations between the unknown mesh-point velocity (u, v) at $(0, 0)$ and the measured velocity (u_k, v_k) at (ξ_k, η_k), as follows,

$$u_k = u + \frac{\partial u}{\partial x}\xi_k + \frac{\partial u}{\partial y}\eta_k, \tag{1}$$

$$v_k = v + \frac{\partial v}{\partial x}\xi_k + \frac{\partial v}{\partial y}\eta_k, \tag{2}$$

the unknown variables $(u, \partial u/\partial x, \partial u/\partial y, v, \partial v/\partial x$ and $\partial v/\partial y)$ at each of the mesh points are determined from 4–30 sets of the measurements (u_k, v_k, ξ_k and η_k) by means of the least-squares method; that is, they are so evaluated that the squares of the difference between both sides of (1) and (2) take their smallest values; thus producing the two components of the mesh-point velocity.

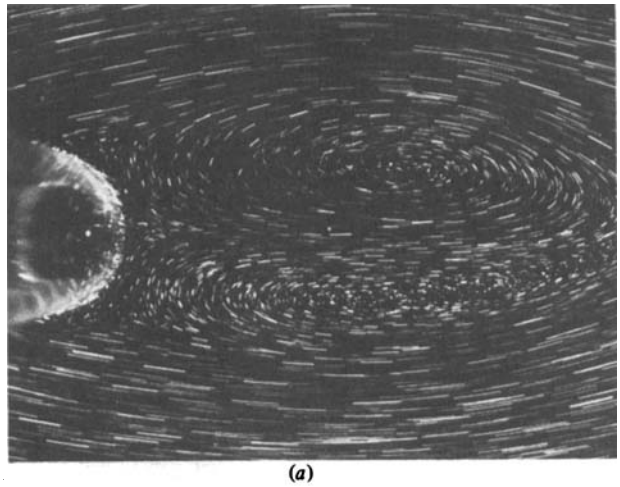

(*a*)

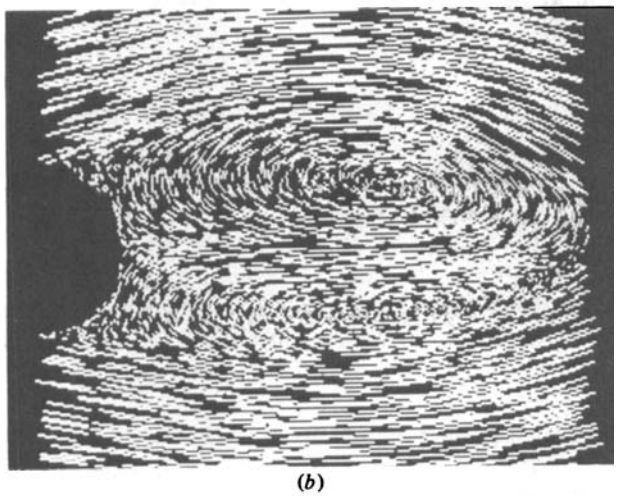

(*b*)

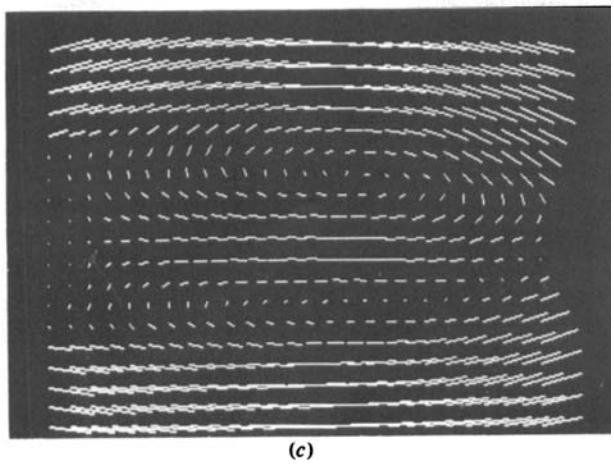

(*c*)

FIGURE 4. An example of measured velocity distribution: (*a*) photographed; (*b*) reproduced on the CRT display of the computer; (*c*) interpolated mesh-point distribution.

The mesh interval is fixed at about $\frac{1}{6}$–$\frac{1}{8}$ of the cylinder diameter as a result of trial calculations of various kinds. First, it was confirmed that, in order to decrease mathematical errors (see § 4) introduced by this linear interpolation, the interpolating area should be extended so far that every one of the four quadrants centred on the mesh point concerned covers at least one measurement of a velocity vector. Secondly, while preserving this condition, and assuming that the area should be circular, an examination was made to establish the minimal radius requred at each mesh point. The results of using various mesh intervals showed that at about 80 % of the mesh points this radius remained within a certain length, and that the scatter was quite normal within these mesh points. This length corresponded to $\frac{1}{12}$–$\frac{1}{16}$ cylinder diameter, and we regarded the doubled radius as an appropriate mesh interval.

Figure 4 (*c*) shows an example of mesh-point distribution of velocity derived from (*b*) in the same figure.

2.4. *Stream function, vorticity, pressure*

The stream function at the mesh point P in figure 5 is

$$\Psi_P = \Psi_O + \int_O^P (u\,dy - v\,dx), \tag{3}$$

were Ψ_O is that for the origin O. Then the mesh-point distribution of the stream function can be calculated by means of iterative integrations of (3), if the initial value Ψ_O and the location of the origin are provided. In our case, the integration of the equation is iterated by means of a trapezoid approximation, and is initiated from a mesh point located in the centre of the computing area in order to minimize the accumulation of integral errors. The initial value is usually supposed to be zero. As regards the integral route, we adopted the method illustrated in figure 6, namely, for the mesh points along the two axes crossing at the origin, we integrated in either the x- or y-direction only, and for all the others the two values integrated in the x- and y-direction are arithmetically averaged.

The vorticity distribution is calculated from that of the mesh-point velocity, with the aid of finite-difference approximation of the definitive formula expressed in two-dimensional form. At a mesh point (i, j) the vorticity ω_{ij} is

$$\omega_{ij} = -\frac{u_{ij+\frac{1}{2}} - u_{ij-\frac{1}{2}}}{\delta y} + \frac{v_{i+\frac{1}{2}j} - v_{i-\frac{1}{2}j}}{\delta x}, \tag{4}$$

where δx and δy are the mesh intervals in the x- and y-directions respectively; and in our calculations it is always the case that $\delta x = \delta y$. The velocity components suffixed with $\frac{1}{2}$ correspond to those equidistant from the relevant two mesh points, and they are evaluated by arithmetically averaged values. It should be remarked in passing that neither vorticity nor pressure are calculated along the four edgelines of the grid area because of the restriction of the finite-difference approximation.

The distribution of pressure is obtained from a series of numerical integrations of the steady Navier–Stokes equation in two-dimensional form; that is

$$u\frac{\partial u}{\partial x} + v\frac{\partial u}{\partial y} = -\frac{1}{\rho}\frac{\partial p}{\partial x} + \nu\left(\frac{\partial^2 u}{\partial x^2} + \frac{\partial^2 u}{\partial y^2}\right), \tag{5}$$

$$u\frac{\partial v}{\partial x} + v\frac{\partial v}{\partial y} = -\frac{1}{\rho}\frac{\partial p}{\partial y} + \nu\left(\frac{\partial^2 v}{\partial x^2} + \frac{\partial^2 v}{\partial y^2}\right). \tag{6}$$

In these equations the pressure gradients $\partial p/\partial x$ and $\partial p/\partial y$ are computed first from the measured values of other terms, among which all the derivatives of u and v are

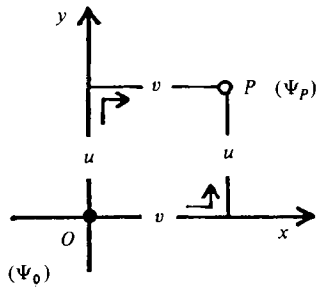

FIGURE 5.

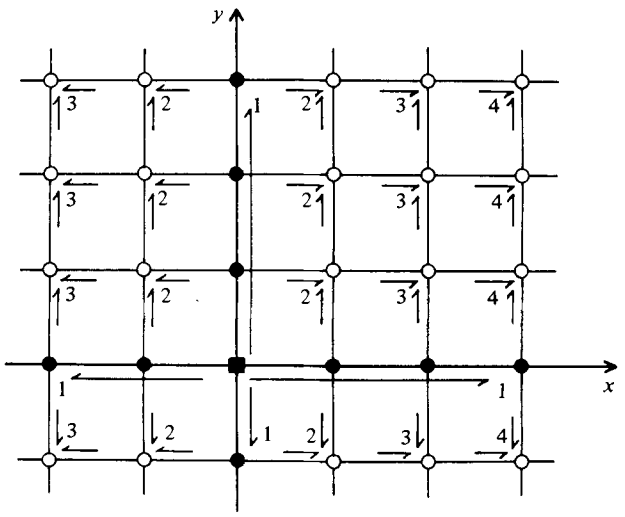

FIGURE 6.

FIGURE 5. Definition of stream function.

FIGURE 6. Portion of mesh points showing integral routes of stream function and pressure. ■, Starting point ($\Psi_O = 0$); ●, integration in x- or y-direction; ○, integration in x- and y-direction (averaged).

evaluated through finite-difference approximation. Then the integration of these pressure gradients are iterated from the starting point situated in the centre of the computing area. The initial value of the pressure is supposed to be ρU_∞^2, where ρ is the density of the fluid and U_∞ the moving speed of the towing carriage (i.e. that of the test cylinder). The integral route is subject to the method illustrated in figure 6 except inside the cylinder.

All the calculations of stream function, vorticity and pressure are normalized according to the following formulae:

$$\Psi^* = \frac{\Psi}{U_\infty d}, \quad \omega^* = \frac{\omega}{U_\infty/d}, \quad p^* = \frac{p}{\rho U_\infty^2}, \tag{7}$$

where d is the diameter of the cylinder. These normalized parameters are linearly interpolated between every two adjacent mesh points, and thereby a number of contour lines are drawn for each of the parameters. The contour lines as well as the relevant velocity profiles are usually presented on the CRT display of the computer, which has 512×256 image dots.

3. Results of calculations

The first example is a series of flow-visualization pictures showing the development of a twin vortex, formed behind a circular cylinder that has been impulsively accelerated to constant speed. They are shown in figure 7 together with the passage of time after the start of motion of the cylinder. The respective distributions of stream function, vorticity and pressure in this unsteady twin-vortex flow are shown in figures 8, 9 and 10. Table 1 is a summary of the parameters employed in the flow-visualization experiment and numerical calculations.

The second example refers to the process of vortex shedding with respect to a Kármán vortex street, generated behind a circular cylinder moving at constant speed. The photographic images are given in figure 11. Figures 12, 13 and 14 show the respective distributions of stream function, vorticity and pressure in this steady-state Kármán vortex flow. The time interval between every two photographs is 3·30 s which is equivalent to about $\frac{1}{8}$ of the period of vortex shedding. Table 2 is a summary of the parameters.

The following is an examination of our experimental results, through which some aspects related to the behaviour and the nature of these two types of flow will be clarified with quantitative support.

3.1. *Stream function*

The two sets of streamline configurations (figures 8 and 12) show a reasonable agreement with their respective originals (figures 7 and 11), even in a cross-flow regime, which is proof of satisfying accuracy with respect to the vectorial aspect of a stream line. As regards the results of the unsteady twin-vortex experiment, it is recognized that asymmetry of the flow came about at a rather early stage of the development as well as that the amount of fluid circulating inside the vortices has hardly changed in the course of this run.

3.2. *Vorticity*

Throughout the vorticity distributions of figures 9 and 13, one understands clearly on numerical grounds the concentration of vorticity in the neighbourhood of the cylinder, as well as its diffusion and decrement downstream. In the results of the Kármán-vortex experiment (figure 13) one can follow the shedding process of vorticity: one of the standing vortex pair concentrated on either side of the cylinder, restraining alternately the spread of the other, starts to divide itself into two, which leads to the vortex shedding. In the results of the unsteady twin-vortex experiment (figure 9) it is found that stage (*d*) presents necks in contour lines of large vorticity, so that it is apparent that the vortex shedding is about to begin.

3.3. *Pressure*

The equipressure-line configurations of the unsteady twin vortex (figure 10) show how the low-pressure part spreads out in the rear of the cylinder and the pressure gradient around it becomes gentle as the twin vortex grows. The results of the Kármán-vortex flow (figure 14) do not show this correspondence between vortex-forming regions and those of low pressure, because these distributions are calculated from the mesh-point velocity compounded with the moving speed U_∞ of the cylinder. We tried therefore to recalculate the distributions of stream function from this compounded mesh-point velocity. The calculation results are illustrated in figure 15, and these demonstrate the well-known phenomenon of pressure dropping toward the centre of curvature of the streamlines.

3.4. *Comparison with results of previously published experimental investigations and theoretical calculations*

The closed wake length of the unsteady twin vortex at $Re = 100$ is measured from the streamline $\Psi^* = 0$ presented in figures 8(*b–d*), and is compared with the results of theoretical calculations by Son & Hanratty (1969) and Collins & Dennis (1973), as well as experimental data by Honji & Taneda (1969) and Bouard & Coutanceau (1980). All of these results are illustrated in figure 16. Both the experimental values,

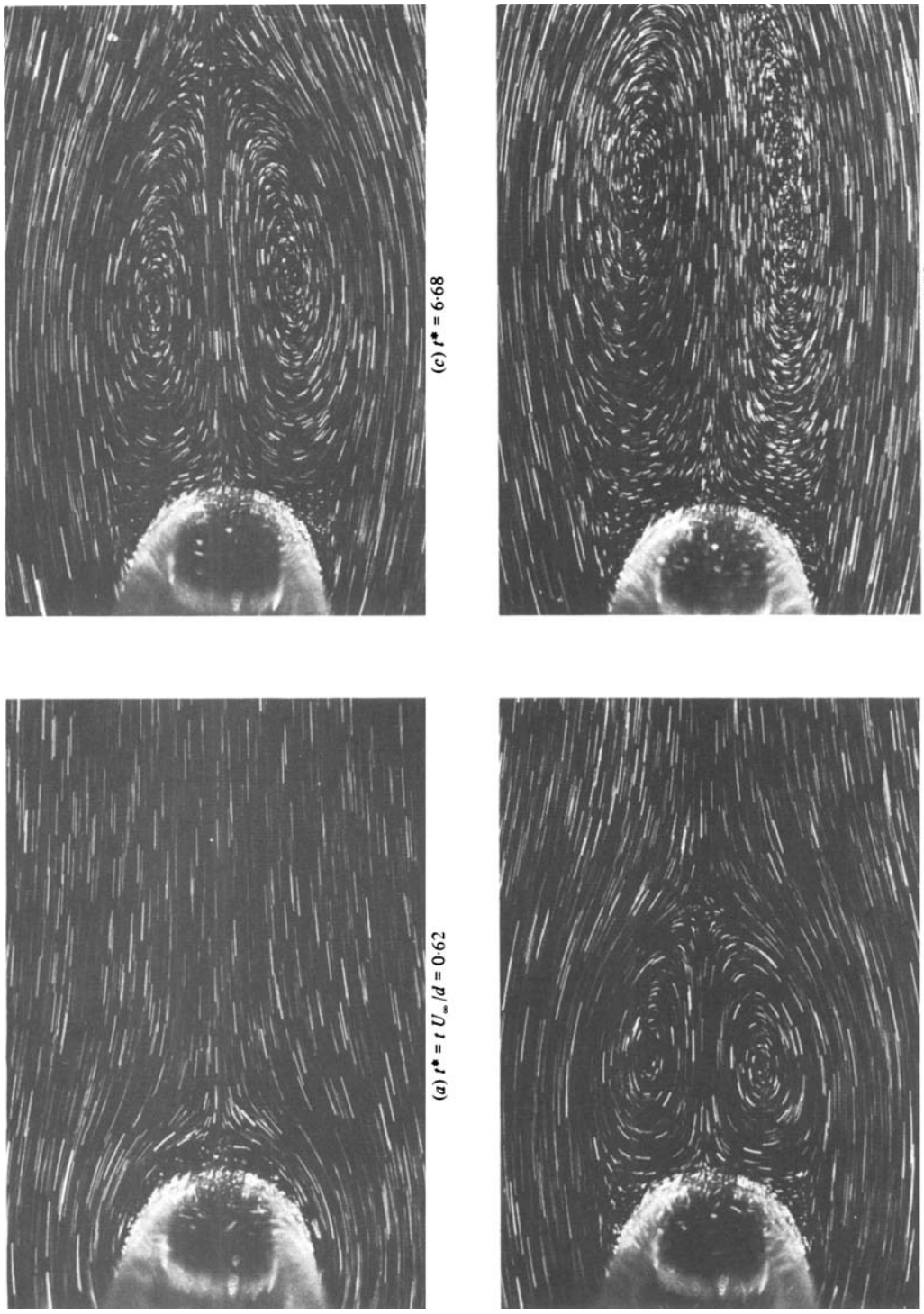

FIGURE 1. Development of an unsteady twin vortex behind a circular cylinder that has been impulsively accelerated to constant speed ($d = 30{\cdot}5$ mm, $U_\infty = 7{\cdot}25$ mm/s, $Re = 200$).

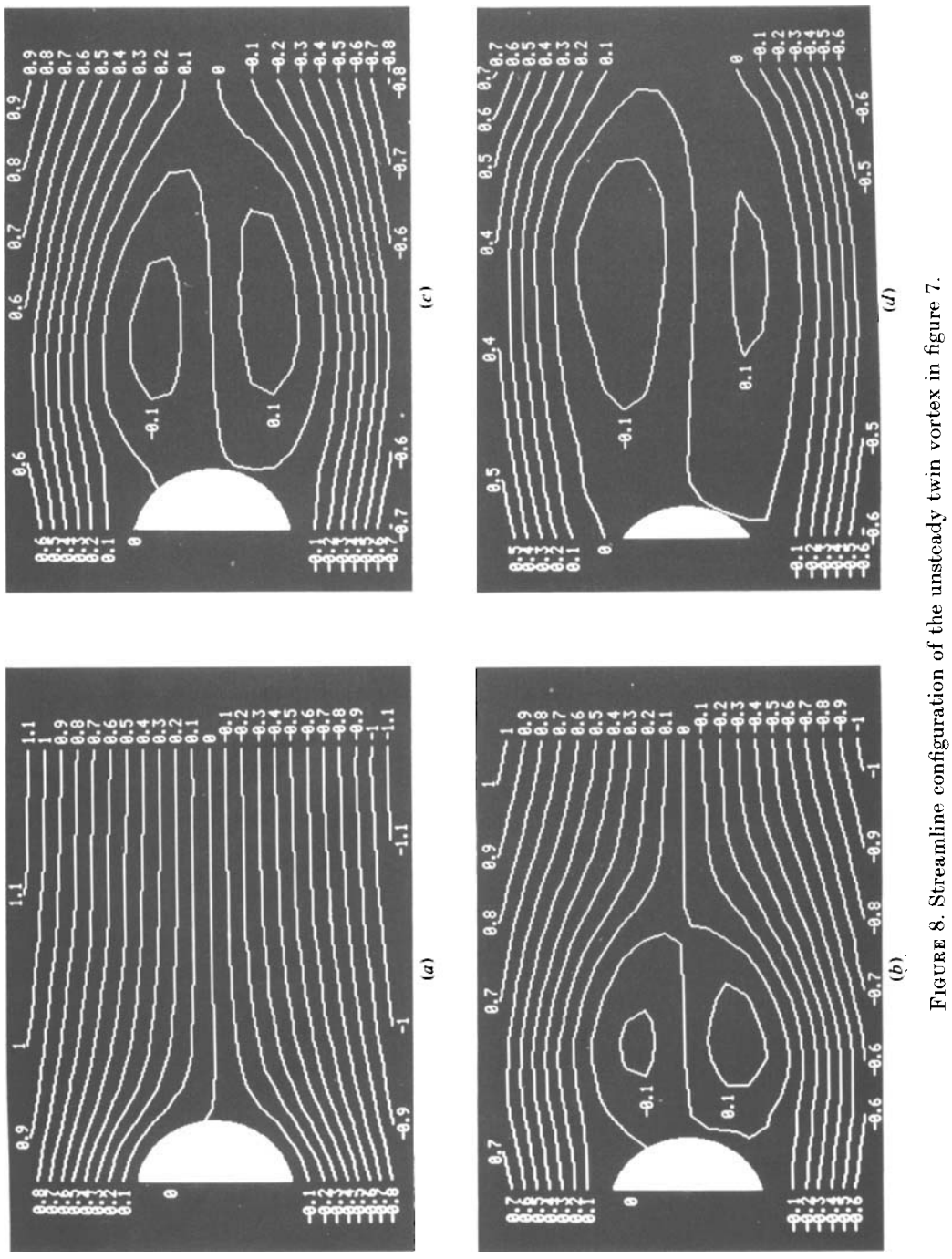

FIGURE 8. Streamline configuration of the unsteady twin vortex in figure 7.

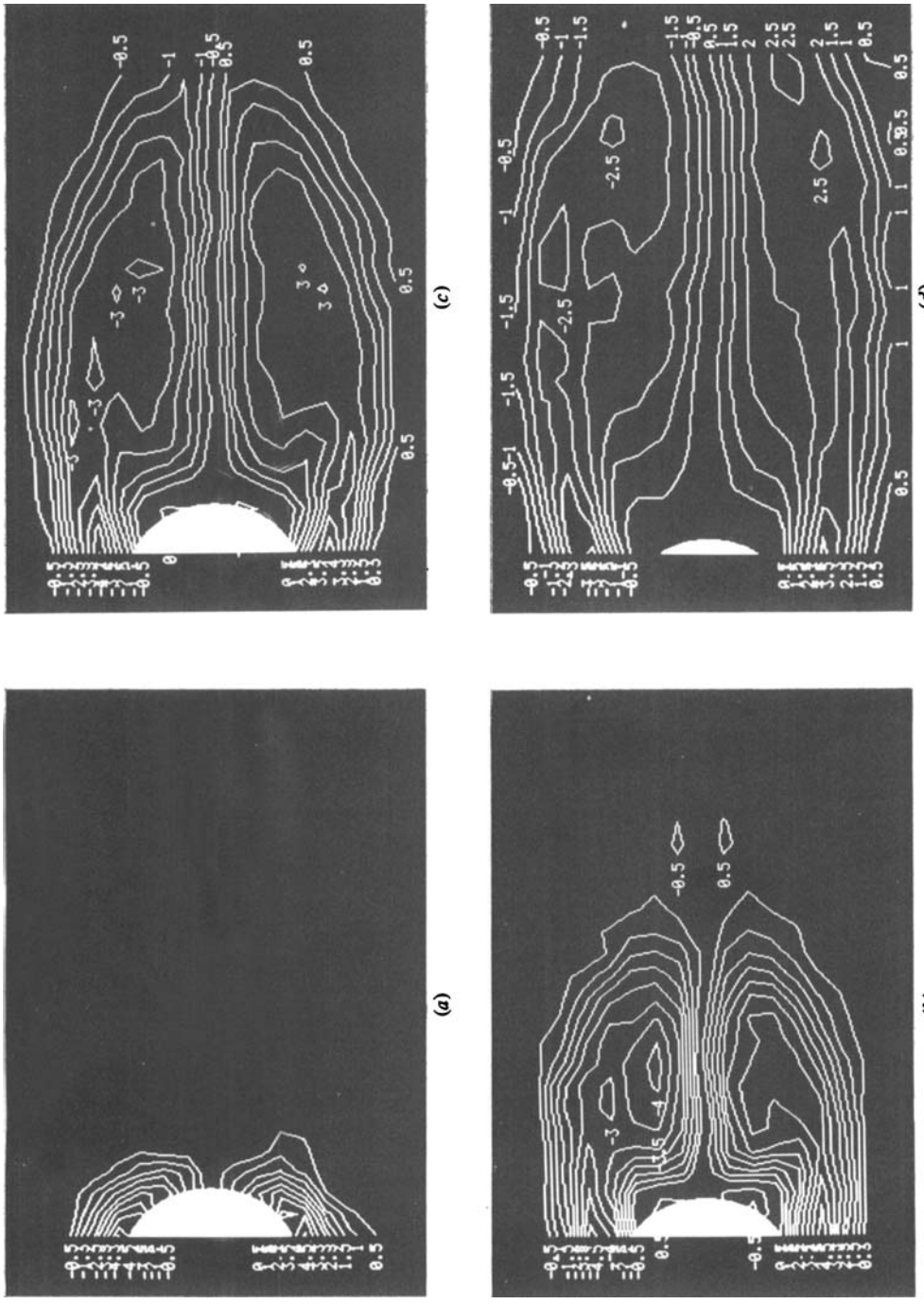

FIGURE 9. Vorticity distribution of the unsteady twin vortex in figure 7.

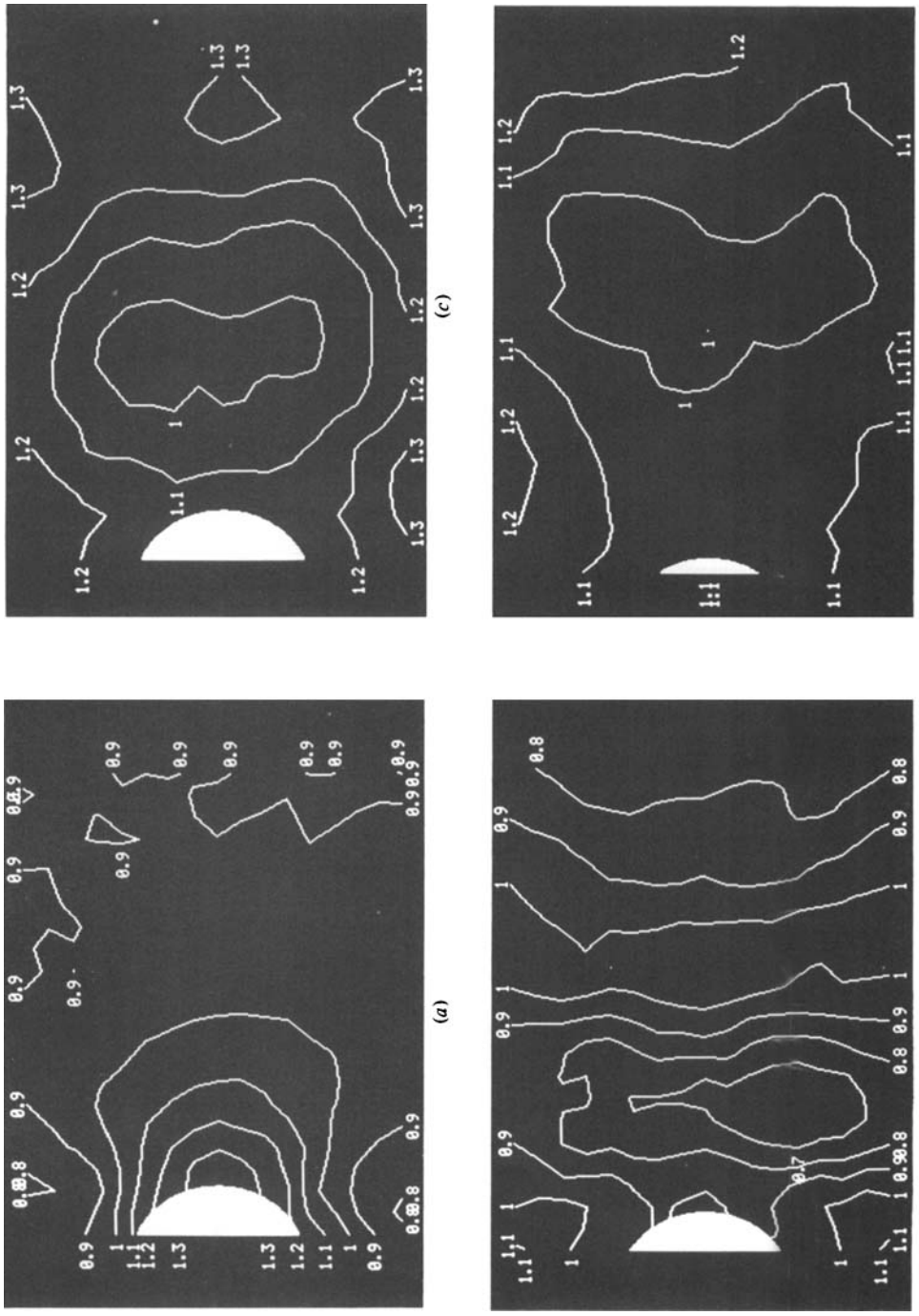

FIGURE 10. Pressure distribution of the unsteady twin vortex in figure 7.

Diameter of cylinder	30·5 mm
Moving speed of cylinder	7·25 mm/s
Reynolds number	200
Position of camera	fixed in relation to cylinder
Exposure time	0·90 s
Mesh interval	$\delta x = \delta y = 3{\cdot}92$ mm
Number of mesh points	19×25 (u, v, Ψ)
	17×23 (ω, p)

TABLE 1. Summary of the parameters of the unsteady twin-vortex experiment (figures 7 and 10)

because of the asymmetry of flow, and the theoretical ones, because of the large size of the meshes away from the cylinder, are inaccurate to some extent, though the former are about 10% larger than the latter in the last stage of comparison. We consider that this is because the unsteady twin vortex produced in the experiments loses its symmetry from early in the run and has a growing tendency toward shedding.

Figure 17 shows streamline configurations at $t^*(= tU_\infty/d) = 2{\cdot}65$ presented in the theoretical calculation by Son & Hanratty (1969) and at $t^* = 2{\cdot}02$ by Patel (1976). These coincide satisfactorily with our experimental result for about the same time duration ($t^* = 3{\cdot}66$, figure 8*b*) as concerns the location of vortex centres and the geometrical configuration of the streamlines, as well as the numerical values of Ψ^*. This is because the comparison is made rather soon after the start of motion of the cylinder.

4. Estimation of errors

There are some potential problems regarding the accuracy of our measurements and calculations:

(i) traceability of aluminium particles;
(ii) errors in measuring particle pathlines on the photograph;
(iii) errors in measuring exposure time of the camera;
(iv) velocity evolution during the exposure time;
(v) errors in numerical calculations.

From among these, the termination error of the computer included within (v) is not discussed here because it is too small to take into account.

4.1. *Traceability of particles*

In spite of a specific gravity of 2·7, the aluminium particles used in the present experiment descend in water at a very small sedimentation rate because they are as small as 2–7 μm in length. According to Stokes' resistance law, this rate is approximately 20 μm/s provided that the particle is a sphere of 5 μm in diameter and the water temperature is 15 °C. In our experiments the acceleration rate of fluid in a horizontal direction is 10^{-3} m/s^2 at most, which is much smaller than that of gravity. The particles are consequently considered to trace the motion of the fluid closely.

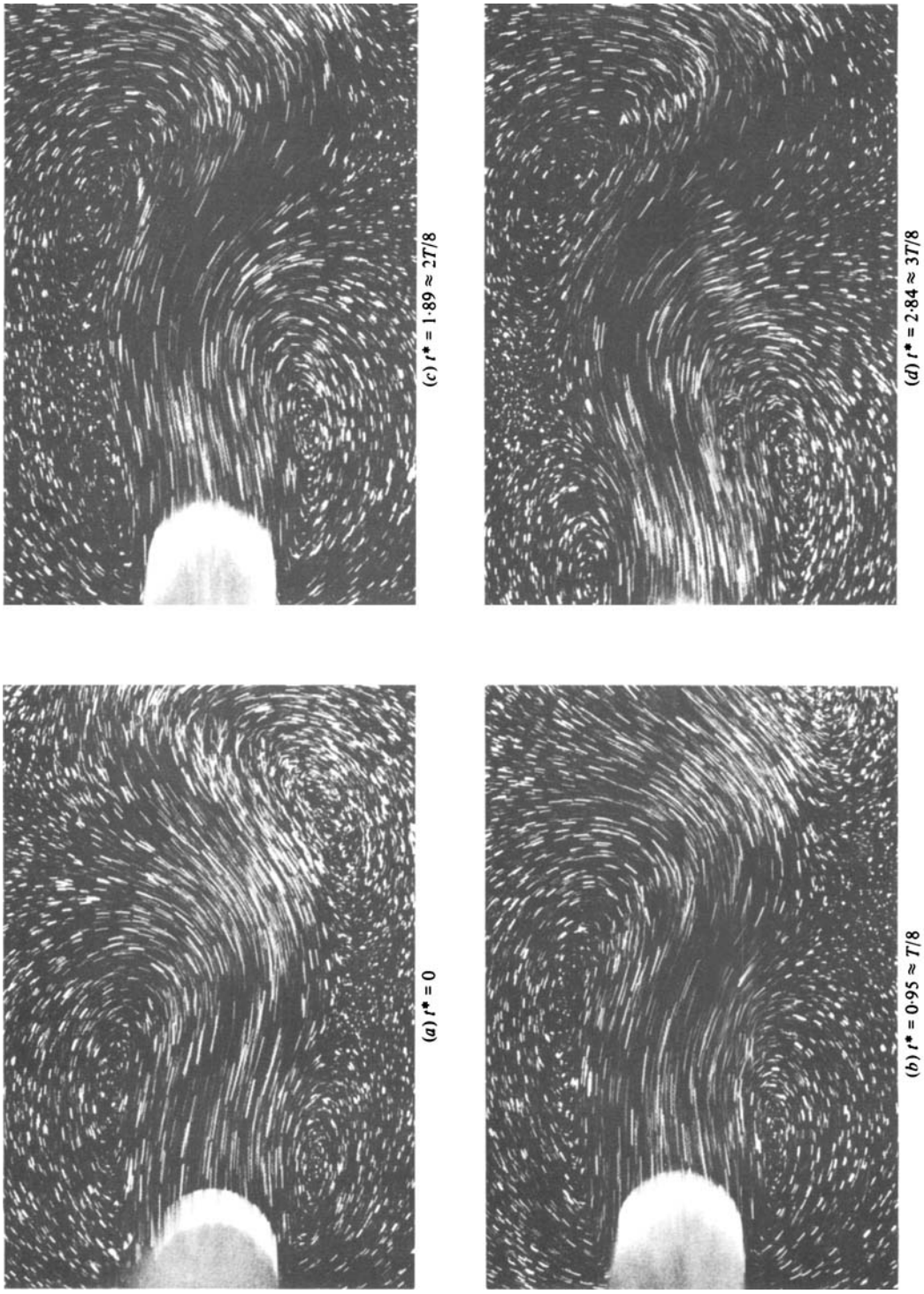

FIGURE 11. Process of vortex shedding in a Kármán vortex street generated behind a circular cylinder moving at constant speed ($d = 19{\cdot}5$ mm, $U_\infty = 5{\cdot}59$ mm/s, $Re = 100$).

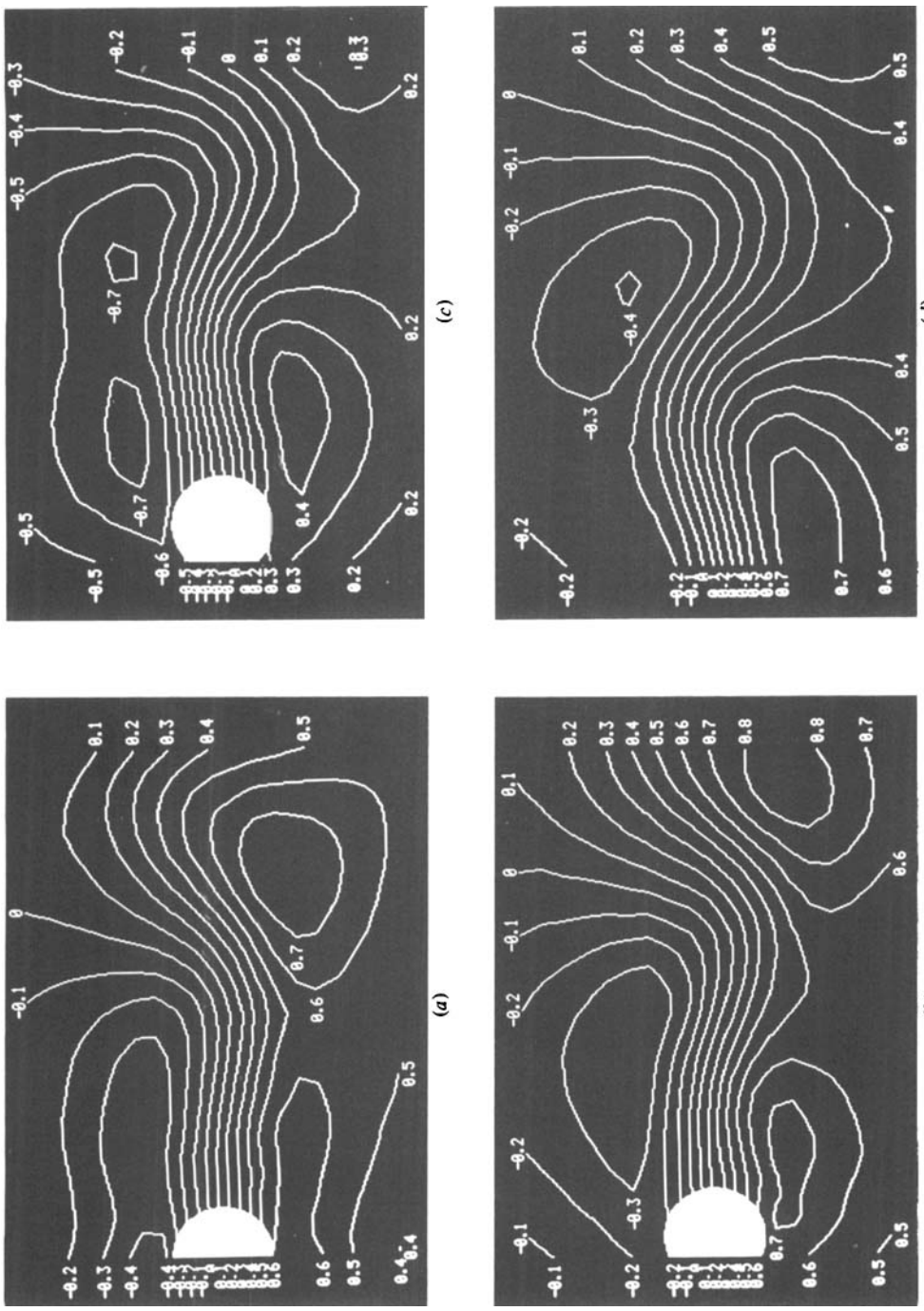

FIGURE 12. Streamline configuration of the Kármán vortex in figure 11.

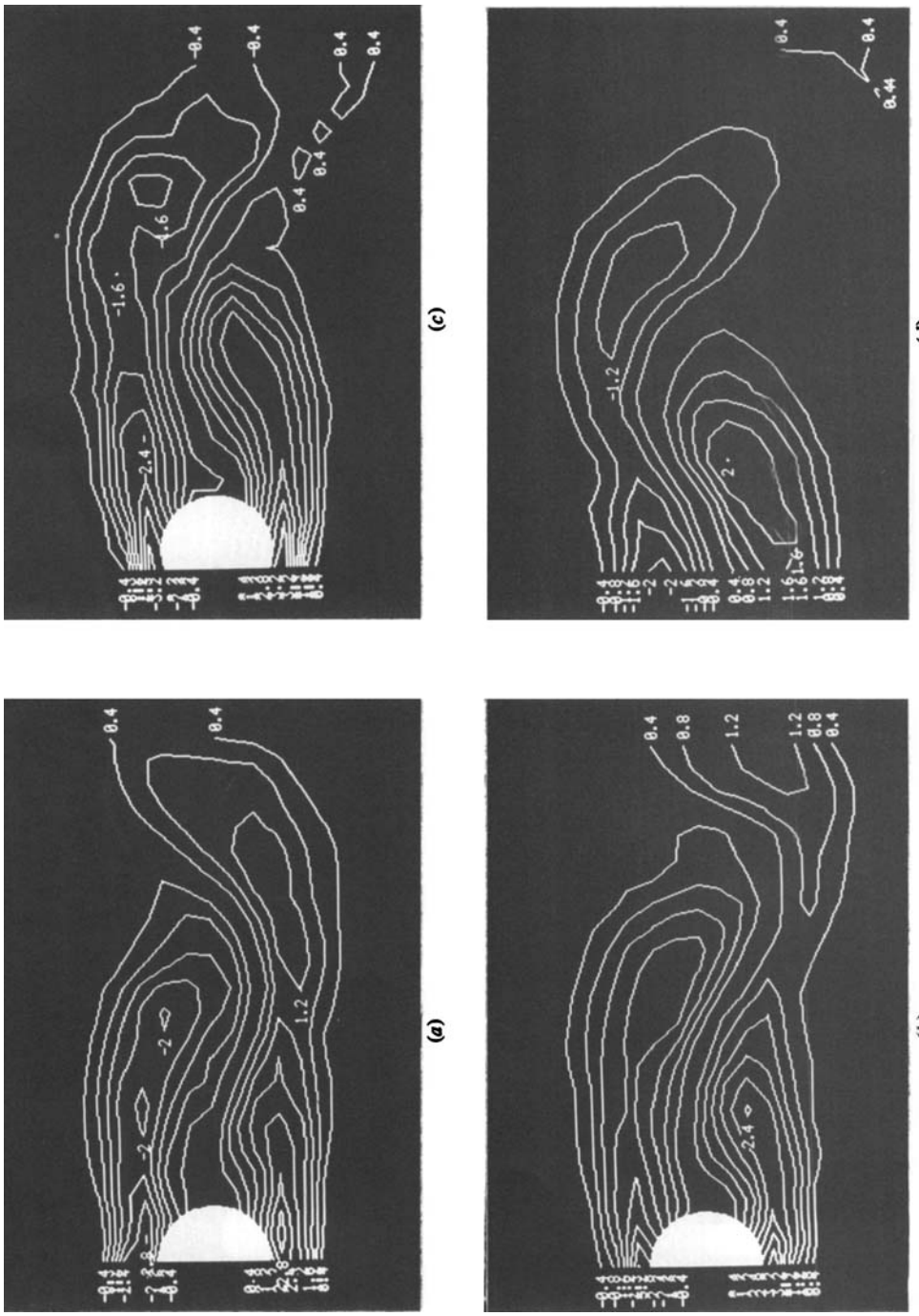

FIGURE 13. Vorticity distribution of the Kármán vortex in figure 11.

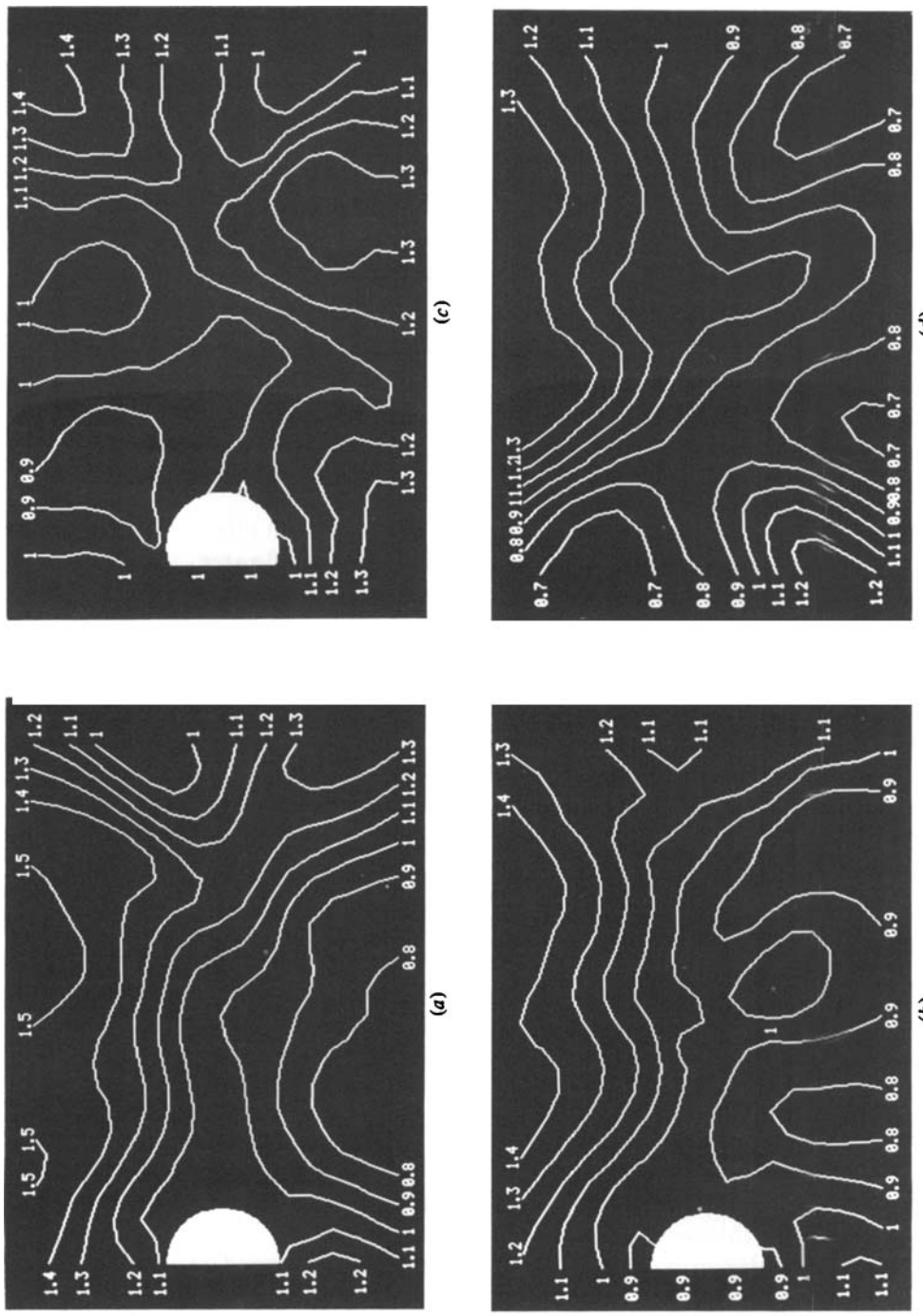

FIGURE 14. Pressure distribution of the Kármán vortex in figure 11.

Diameter of cylinder	19·5 mm
Moving speed of cylinder	5·59 mm/s
Reynolds number	100
Position of camera	fixed in relation to fluid
Exposure time	0·90 s
Photographing interval	3·30 s ($\approx \frac{1}{8}T$)
Mesh interval	$\delta x = \delta y = 3{\cdot}97$ mm
Number of mesh points	19×26 (u, v, Ψ)
	17×24 (ω, p)

(T = period of vortex shedding)

TABLE 2. Summary of the parameters of the Kármán-vortex experiment (figures 11 and 15)

4.2. *Errors in measuring particle pathlines on the photograph*

These can be subdivided into four categories:

(i) distortion of photographic images owing to the optical effect of lenses of the photographic apparatus as well as to the refractive effect of water;

(ii) effect of the thickness of the lighting plane;

(iii) expansion or contraction of photographic paper owing to a change in room temperature or humidity;

(iv) measurement errors in operating the digitizing tablet caused by perceptual errors on the part of the operator or instrumental inaccuracy.

From among these (i), the distortion of photographic images, is not discussed here because, as is mentioned in § 2, calibration is made for every pair of x- and y-coordinates noted on the photograph. As for (iii), the expansion or contraction of photographic paper, it has been confirmed in the process of the calibration that the plastic-coated paper employed here causes hardly any problems for the measurement. It is therefore the effects of (ii) and (iv) that will be discussed here.

4.2.1. *Effect of the thickness of the lighting plane.* It is at two points in the photographic field of the camera that the thickness of the lighting plane affects measurement results most seriously, that is, at the bottom of the right and left edges of the field, because both the thickness itself and the angle of vision of the camera take their largest values there. Supposing the camera is fixed at the lowest position in common use, where the vertical cross-section at these two points is illustrated in figure 18, the computed value of the displacement δ noted in this figure is about 1·0 mm. On the other hand, when evaluating the velocity gradients ($\partial u/\partial x$, $\partial u/\partial y$, $\partial v/\partial x$, $\partial v/\partial y$) at each of the mesh points by means of a linear approximation, the maximal gradient turns out to be less than 0·2 s^{-1}. The maximal error of velocity vectors caused by this displacement is therefore 0·2 mm/s.

4.2.2. *Measurement errors in operating the digitizing tablet caused by perceptual errors on the part of the operator or instrumental inaccuracy.* For the purpose of estimating the liability to errors of this kind occurring with our experimental technique, the towing water tank of figure 1 is re-employed without setting the cylinder on the carriage. The aluminium particles, suspended in water and kept carefully in a stationary state, are photographed with the same camera as is used in the experiments, fixed to the towing carriage moving at constant speed. Then the length of every particle path on the resulting photographs is measured by the use of the digitizing tablet. The results are at most 0·4 mm longer or shorter than those established by

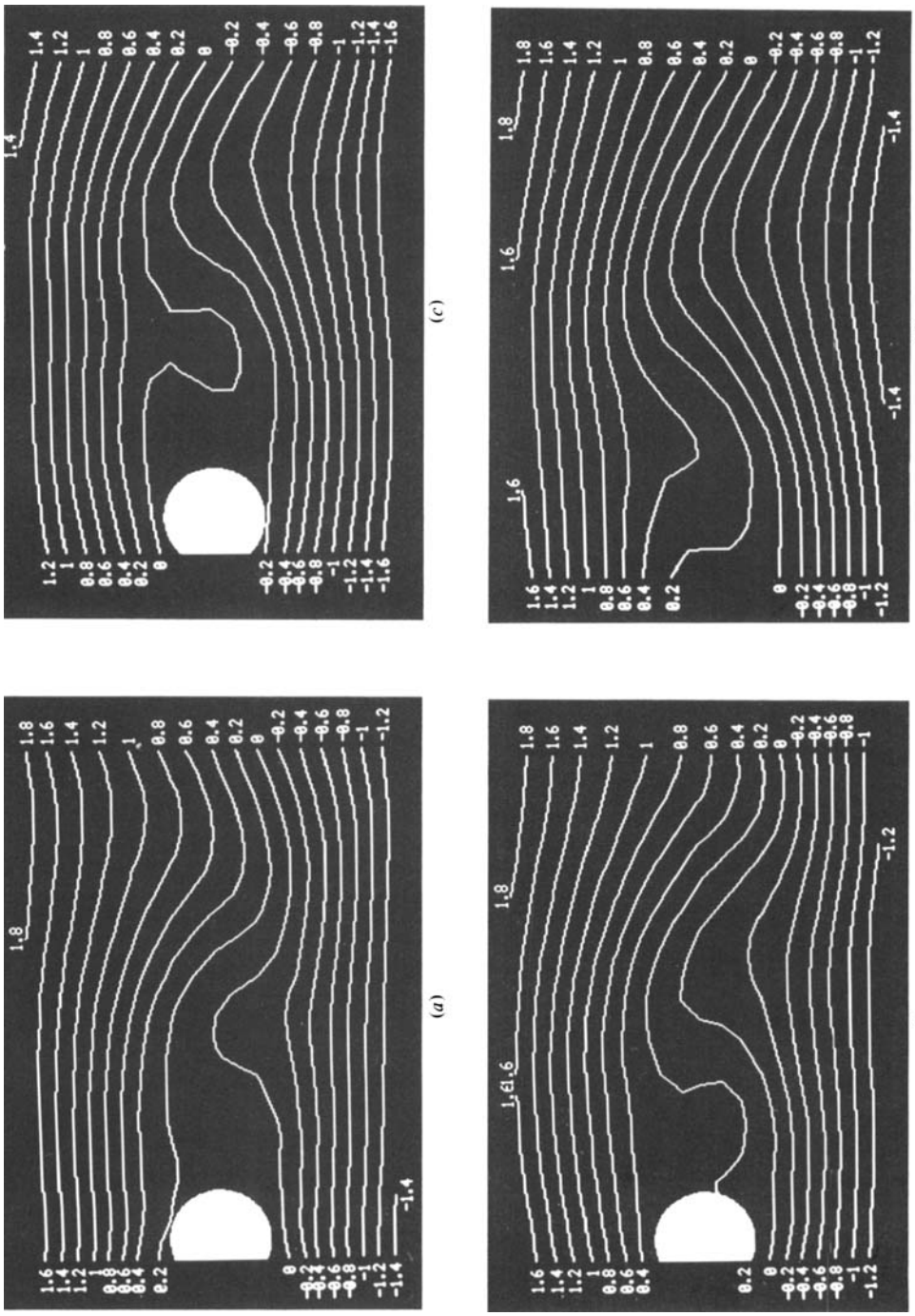

FIGURE 15. Moving streamline configuration of the Kármán vortex in figure 11.

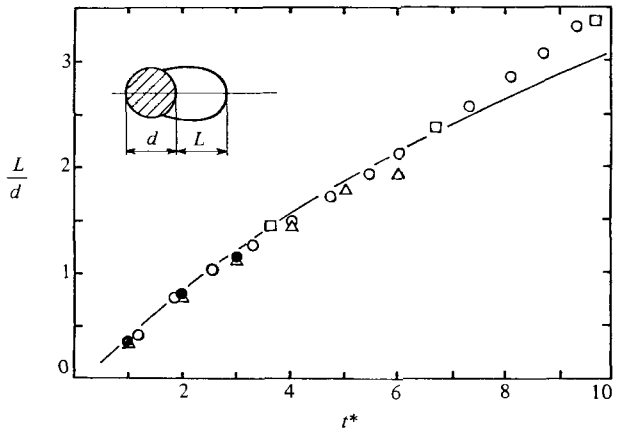

FIGURE 16. Time development of closed wake length. Theoretical values: ——, Son & Hanratty (1969); △, Collins & Dennis (1973). Experimental values: ○, Honji & Taneda (1969); ●, Bouard & Coutanceau (1980); □, present study.

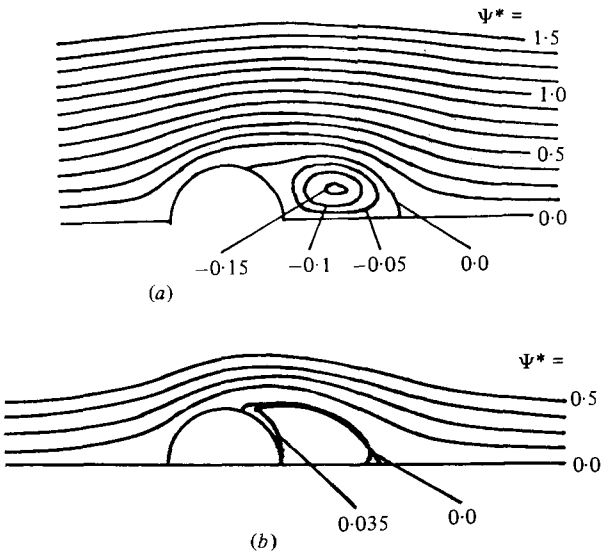

FIGURE 17. Streamline configurations at $Re = 200$ derived from theoretical calculations: (*a*) Son & Hanratty (1969) ($t^* = 2{\cdot}65$); (*b*) Patel (1976), ($t^* = 2{\cdot}02$).

a more objective estimation based on the measured moving speed of the towing carriage, the exposure time of the camera, the degree of magnification of the photographic image, and the optical distortion introduced into it. This difference in length corresponds to 0·17 mm on the real scale. Since the exposure time of the camera is always 0·90 s in the course of this examination, the maximal measurement error of velocity vectors discussed here is within 0·2 mm/s.

4.2.3. *Effect of measurement error on calculated results.* From the above, we come to the conclusion that the maximal measurement error of velocity vectors amounts to 0·4 mm/s. It is probable therefore that the measurement of short particle paths of 2–3 mm or less might be considerably affected by this degree of error. In order to examine the effect, artifical error values within $\pm 0{\cdot}4$ mm/s are added in random order to every measurement of velocity vectors, and each of the parameters

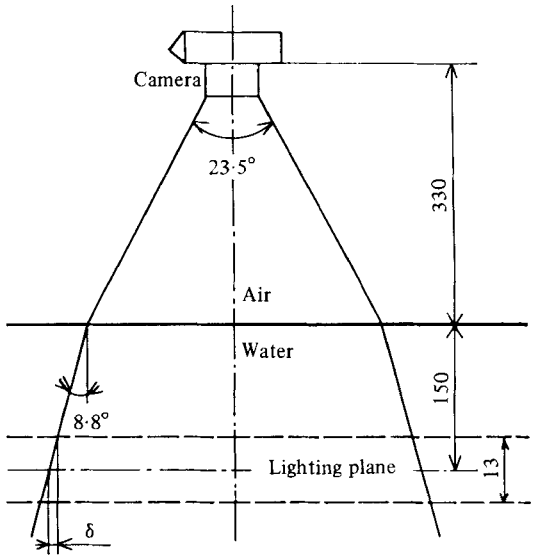

FIGURE 18. Vertical cross-section of the water tank where the thickness of the lighting plane is greatest. (Unit of length: mm.)

calculated from this 'renewed' velocity distribution is compared with the original, which contains no artificial errors. The error values are supposed to be subject to a Gaussian distribution. In consequence of this comparison, some of the components of the interpolated mesh-point velocity have changed by about 10%, though the change in calculations of stream function, vorticity and pressure has remained less than 5%.

4.3. *Errors in measuring exposure time of the camera*

The motion of the focal-plane shutter of the camera is recorded by VTR equipment, together with the superimposed visual display of the passage of time. After measuring the exposure time based on this visual display of time, the result is compared with that by means of the electrical measurement explained in § 2. The difference between these two is of the order of 10^{-3} s in the case of our usual exposure time of approximately 0·90 s. Therefore the error rate of the exposure-time measurement is within 1%, whereas that of the velocity-vector measurement is 5% at least. This means that the time-measurement error has hardly any effects on the determination of velocity fields.

4.4. *Velocity evolution during the exposure time*

The exposure time of the camera should be short enough to diminish the effect of nonlinear velocity evolution for its duration, and, at the same time, long enough to avoid the measurement error of particle paths. In our experiment, as a result of some trial calculations, it is fixed at 0·90 s, which corresponds to the minimal required exposure time with which the measurement error of velocity vectors remains within 0·4 mm/s, and (this is very important) the direction of the vectors can be barely determined even in the most-stagnant regions. One of the criteria of the former requirement is the ratio of exposure time to the fluctuation period of the flow. In our experiment on the Kármán vortex at $Re = 100$, the vortex-shedding period is about 25 s, so that the ratio is approximately 28. Considering here the slower velocity evolution in the unsteady twin-vortex flow at $Re = 200$, the velocity fluctuation

during the exposure time does not seem to produce a serious effect on our measurements.

4.5. *Errors in numerical calculations*

The estimation of the errors in this category is carried out in a way similar to that described by Apelt (1958) and Hamielec & Raal (1969) in their numerical calculations of the theoretical analysis.

4.5.1. *Residual of the results calculated by means of the least-squares method.* When interpolating the mesh-point velocity by means of the linear approximation explained in § 2, calculation is also made as to residuals of the results calculated by means of the least-squares method, and the accuracy of the interpolation is estimated from their maximal and root-mean-square values at each of the mesh points. As regards the maximal values of residuals, the effect of the measurement error has exceeded that of the calculation error in many of the small-velocity regions, which results in residuals being more than twice as large as measurements. However, in large-velocity regions in which the interpolated velocity is 3 mm/s or more, the effect of the measurement error decreases and the maximal value of residuals always remains within 40 % of the measurements. This large percentage of around 40 % is generally found at some of the mesh points located near the cylinder. Since the same tendency is found with the root-mean-square values of residuals, the interpolation of mesh-point velocity is considered to be relatively inaccurate in the neighbourhood of the cylinder.

4.5.2. *Variation of integrated parameters according to integral route.* The evaluation of stream function and pressure at most of the mesh points is carried out by averaging two values integrated in the x- and y-directions, as is explained in connection with figure 6. We tried therefore to estimate the integral error from the difference between these two values of integration.

(*a*) *Integral error in calculating distributions of stream function.* Table 3 shows the results of integration concerning the stream function. Obviously the integral error of the Kármán-vortex experiment is, on the whole, larger than that of the unsteady twin-vortex experiment. Within the results of the latter, the degree of error decreases with the passage of time. As a result of examining the distribution of errors, one finds that it is with one or two examples of the eight that large values of integral error stand out in the neighbourhood of the cylinder. With all the others, however, large errors are introduced only at random in small-velocity regions. It is thought from the above that the integral error of the stream function originates mainly from the measurement error of velocity vectors in these regions. It can be said as well that the calculation of the stream function is so accurate that we can take this as adequately established.

(*b*) *Integral error in calculating distributions of pressure.* Table 4 shows the results of integration related to the pressure. The error values are evidently larger here, except that those in the last two stages of the unsteady twin-vortex experiment are comparatively small. Examining the distribution of errors, one sees several regions with large error values spread out in the rear of the cylinder and near the roll-up of vortices. In consideration of the two facts that the time development of flow becomes very slow in the last two stages of our experiment of the unsteady twin vortex and that the flow immediately behind the cylinder is subject to a very rapid change of the velocity field, it is thought that the integral error of the pressure is, for the greater part, due to the neglect of the unsteady terms in the original equations.

4.5.3. *Error estimation by means of the equation of continuity.* The error due to calculation is estimated also by examining the sufficiency of the equation of

		Difference $\delta\Psi^*$	
		Maximal values	Mean values
Unsteady twin vortex	(*a*)	0·053	0·007
	(*b*)	0·060	0·014
	(*c*)	0·044	0·008
	(*d*)	0·035	0·007
Kármán vortex in steady state	(*a*)	0·091	0·016
	(*b*)	0·069	0·013
	(*c*)	0·075	0·013
	(*d*)	0·036	0·010

(*a*)–(*d*) correspond to figures 7 and 11

TABLE 3. Difference $\delta\Psi^*$ between two integrated values of stream function

		Difference δp^*	
		Maximal values	Mean values
Unsteady twin vortex	(*a*)	0·352	0·033
	(*b*)	0·204	0·050
	(*c*)	0·166	0·029
	(*d*)	0·114	0·021
Kármán vortex in steady state	(*a*)	0·388	0·092
	(*b*)	0·386	0·078
	(*c*)	0·341	0·070
	(*d*)	0·286	0·088

(*a*)–(*d*) correspond to figures 7 and 11

TABLE 4. Difference δp^* between two integrated values of pressure

continuity for each of the mesh sections. This sufficiency is judged from the value ϵ, which is defined as follows: for a mesh point (i,j),

$$\epsilon_{ij} = \left| \frac{(\partial u/\partial x)_{ij}\,\delta x\,\delta y + (\partial v/\partial y)_{ij}\,\delta y\,\delta x}{U_\infty\,\delta y} \right|, \tag{8}$$

where the velocity gradients $\partial u/\partial x$ and $\partial v/\partial y$ are evaluated from the distributions of mesh-point velocity with the aid of finite-difference approximation, as is the case in calculating the vorticity. Table 5 shows the distribution of ϵ together with the mean values thereof. Considering here that the maximal error rate of the velocity-vector measurement is more than 3%, one comes to the conclusion that the equation of continuity is well satisfied with respect to the greater part of the mesh sections within the extent of measurement errors. Mesh sections provided with large values of ϵ are found generally in the neighbourhood of the cylinder and the vortex-forming regions. The reason for this is thought to be that the nature of the velocity field around these mesh sections is not susceptible to the linear approximation.

4.5.4. *Calculations with varied mesh intervals.* The mesh interval was reset twice in calculating the parameters in the two examples of the experiments whose original

		Distribution of ϵ (number of mesh points)				Mean values of ϵ %
		0–5 %	5–10 %	10–15 %	15–20 %	
Unsteady twin vortex	(*a*)	338	43	9	1	2·5
	(*b*)	306	70	12	3	3·1
	(*c*)	340	46	4	1	2·5
	(*d*)	367	24	0	0	1·9
Kármán vortex in steady state	(*a*)	322	73	9	4	3·1
	(*b*)	362	36	7	3	2·5
	(*c*)	389	18	1	0	1·9
	(*d*)	359	39	8	2	2·3

(*a*)–(*d*) correspond to figures 7 and 11

TABLE 5. Distribution and mean values of ϵ

	Difference $\delta\Psi^*$			
	Mesh interval	Maximal values	Mean values	Mean values normalized by $\delta x = \delta y$
Twin vortex (*d*)	×2	0·053	0·012	0·006
	×1	0·035	0·007	0·007
	×0·5	0·028	0·004	0·008
Kármán vortex (*d*)	×2	0·092	0·020	0·010
	×1	0·036	0·010	0·010
	×0·5	0·022	0·006	0·011

(*d*) corresponds to figures 7 and 11

TABLE 6. Variation of difference $\delta\Psi^*$ according to mesh interval

images appear in figures 7 (*d*) and 11 (*d*); the first time at twice as long and the second time at half as long. Calculated results derived from the same original are compared with one another and the calculation error is estimated according to the procedure described in the preceding sections.

(*a*) *Stream function.* The variation of distributions of stream function according to mesh interval is illustrated in figure 19. Finer meshes produce a more-detailed description of streamlines, especially when they have large curvatures. Nevertheless, taken as a whole, one might say that the three kinds of results differ only slightly from one other.

Table 6 shows the difference between two integral values of stream function integrated along different routes. From this table, it can be seen that, though the difference $\delta\Psi^*$ decreases with finer meshes, the normalized difference is much the same regardless of mesh intervals. It is concluded also from this that the integral error of the stream function originates mainly from the measurement error.

(*b*) *Vorticity.* The vorticity distributions derived from the calculations of varied mesh intervals are given in figure 20. In the case of the finest mesh, every equivorticity line is drawn minutely, and the peaks of vorticity located on both sides of the cylinder, which are otherwise smoothed out and obscured, come to appear clearly. Except in these regions, however, one finds some unnaturally curved contour lines or unexplained peaks of vorticity. Table 7 shows some of the calculations of ϵ defined

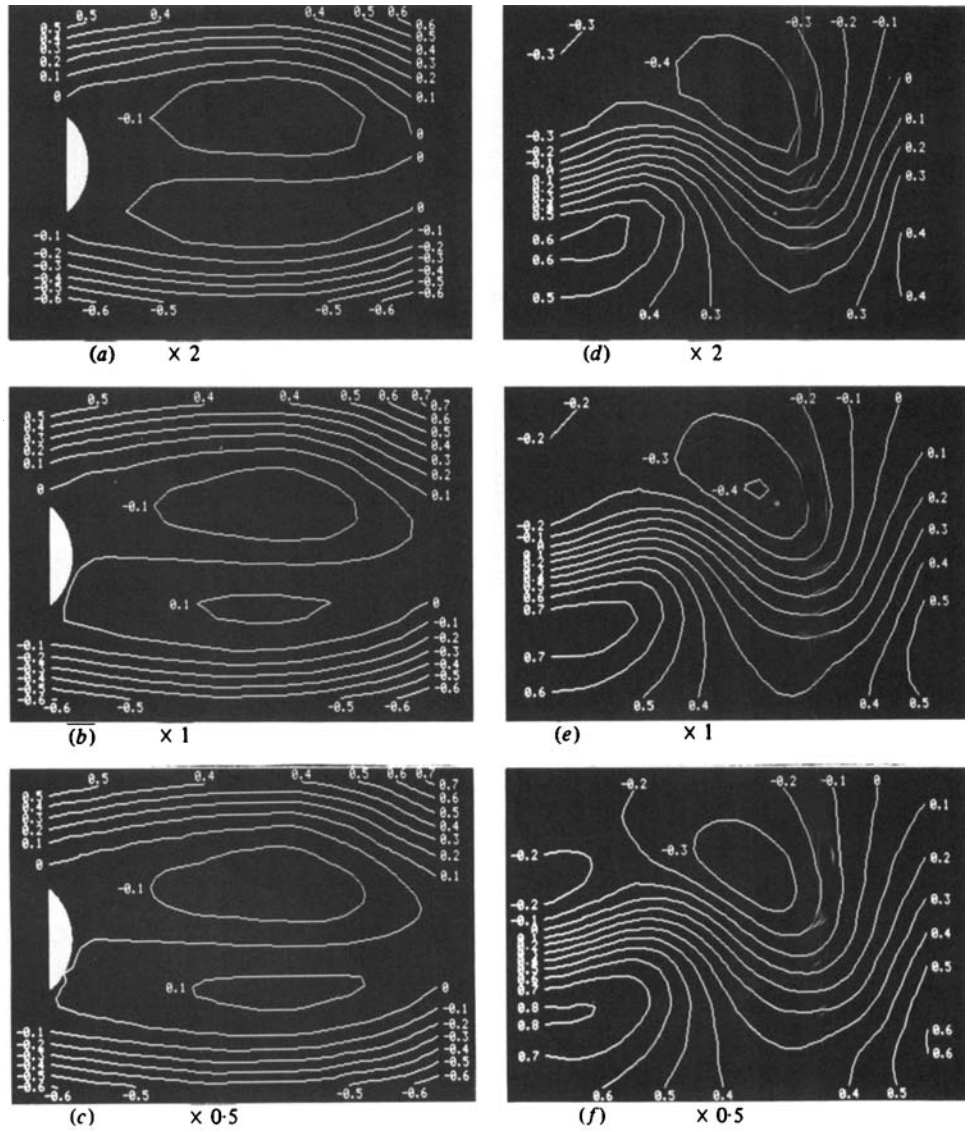

FIGURE 19. Distributions of stream function with varied mesh intervals: (*a*)–(*c*) unsteady twin vortex; (*d*)–(*f*) Kármán vortex.

by (8). This value of ϵ is thought to reflect the accuracy of vorticity, because both ϵ and the vorticity are calculated here from the velocity gradients computed by means of the same finite-difference approximation. It is obvious from this table that the mean value of ϵ is smallest in the case of the original mesh interval. The reason for this is considered to be as follows: some of the computed velocity gradients are greatly affected, in the case of larger meshes, by calculational errors originating from the linear approximation of the velocity field, or, in the opposite case, by the measurement error of velocity vectors. As a result, it might be said that the mesh interval in the present experiment has been properly determined with respect to the calculation of vorticity, though finer meshes are required in some parts.

(*c*) *Pressure.* The variation of pressure distributions according to mesh interval is shown in figure 21. It is clear that the results of the Kármán-vortex experiment present an outstanding change, especially a change in pressure gradients, according

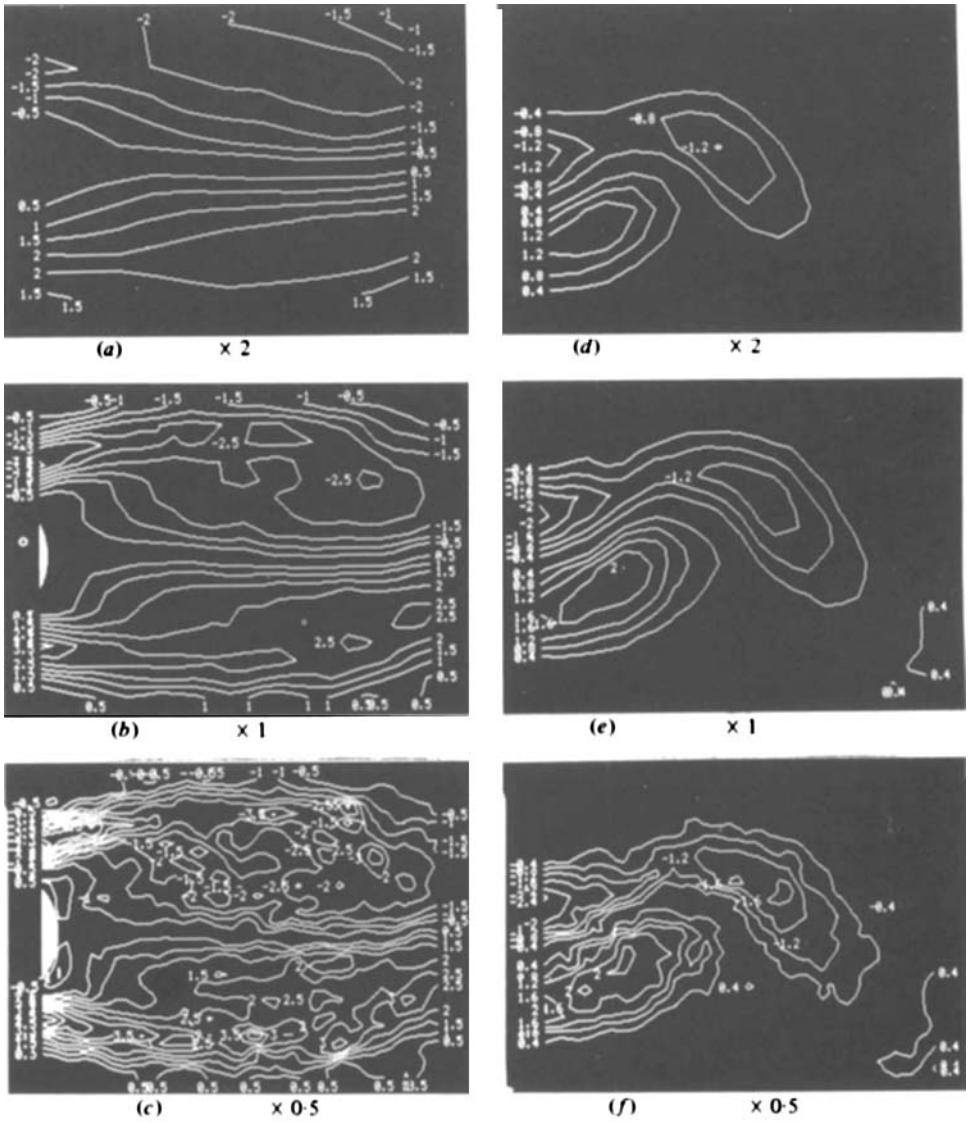

FIGURE 20. Vorticity distributions with varied mesh intervals: (*a*)–(*c*) unsteady twin vortex; (*d*)–(*f*) Kármán vortex.

		Error rate ϵ (%)	
	Mesh interval	Maximal values	Mean values
Twin vortex (*d*)	× 2	8·66	2·67
	× 1	7·92	1·88
	× 0·5	16·1	1·75
Kármán vortex (*d*)	× 2	11·1	2·49
	× 1	10·4	1·86
	× 0·5	11·9	1·79

(*d*) corresponds to figures 7 and 11

TABLE 7. Variation of calculations of ϵ according to mesh interval

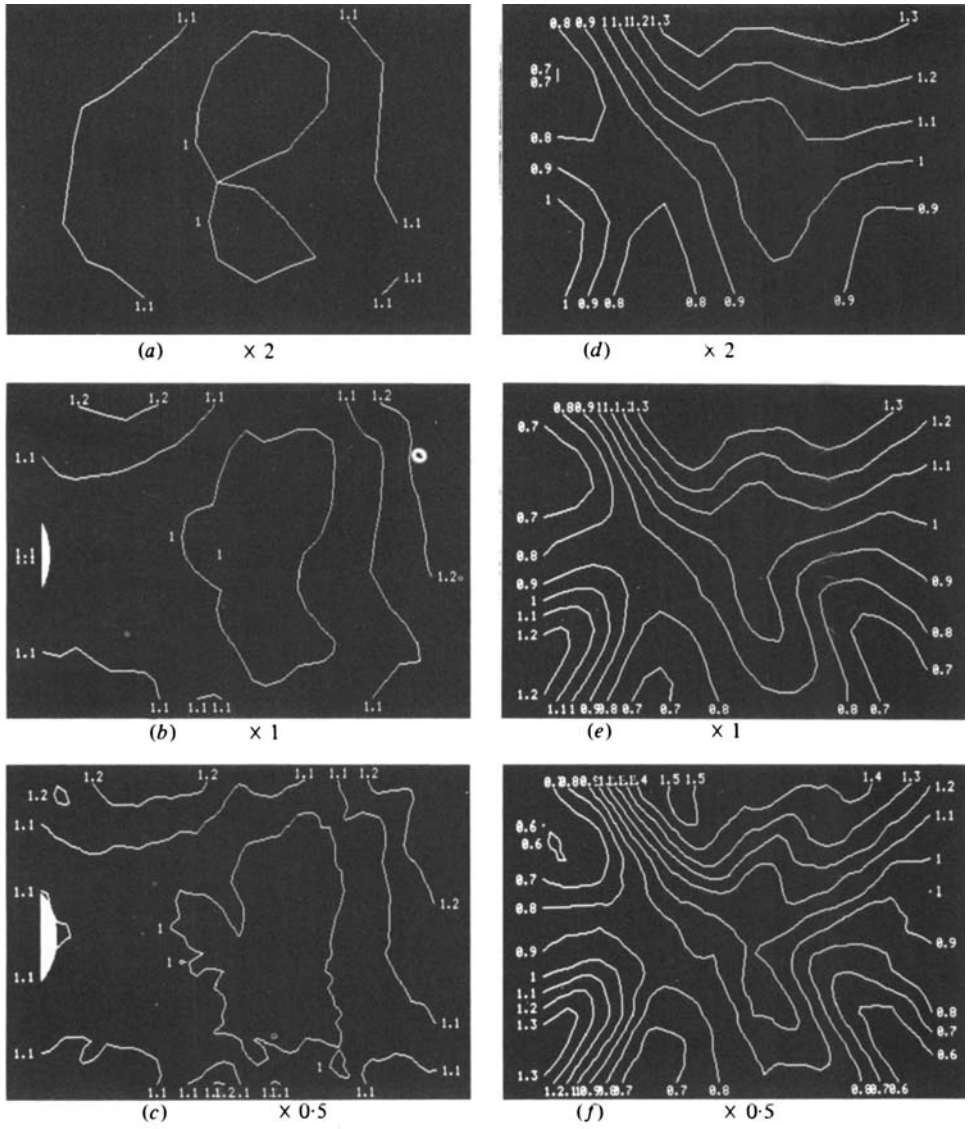

FIGURE 21. Pressure distributions with varied mesh intervals: (*a*)–(*c*) unsteady twin vortex; (*d*)–(*f*) Kármán vortex.

o that in the mesh interval. Since this is not clearly recognized in the results of the nsteady twin-vortex experiment, in which the flow is subject to a very slow change f velocity fields, it is supposed that the calculation of the pressure is strongly affected y the neglect of the unsteady terms in the original equations.

Table 8 shows the difference between two integral values of pressure integrated long different routes. It can be seen from this table that the integral error grows ırger as the mesh grows finer. The reason for this is probably that the calculations f mesh-point velocity incorporate a certain degree of approximation error indepen- ently of mesh intervals, because of the fixed density of velocity vectors distributed ı the photographic image. Consequently the derivatives of velocity components in ıe equations concerned ought to be less accurate with finer meshes, as long as they 'e computed by means of finite-difference approximation.

		Difference δp^*		
	Mesh interval	Maximal values	Mean values	Mean values normalized by $\delta x = \delta y$
Twin vortex (*d*)	×2	0·111	0·026	0·013
	×1	0·114	0·021	0·021
	×0·5	0·147	0·017	0·034
Kármán vortex (*d*)	×2	0·387	0·121	0·061
	×1	0·286	0·088	0·088
	×0·5	0·191	0·055	0·111

(*d*) corresponds to figures 7 and 11

TABLE 8. Variation of difference δp^* according to mesh interval

5. Conclusions

(i) A new system has been developed for evaluating the principal physical parameters of various types of two-dimensional flow, steady or unsteady, with the aid of flow-visualization and image-processing techniques.

(ii) Through the application of this system, instantaneous distributions of velocity, stream function, vorticity and pressure were calculated with reasonable accuracy for two examples of flow past a circular cylinder; one is characterized by an unsteady twin vortex at $Re = 200$ and the other by a Kármán vortex in a steady state at $Re = 100$.

(iii) The results of the unsteady twin-vortex experiment corresponded well with those of previously published experimental investigations and theoretical calculations in the early stages after the start of motion of the cylinder.

(iv) The results of the Kármán-vortex experiment clearly showed the shedding process of vorticity from the neighbourhood of the cylinder and provided numerical support.

(v) The measurement error of velocity vectors evaluated from the flow-visualization pictures was within 0·4 mm/s, which affected the subsequent calculations only to a minor degree.

(vi) As concerns calculation errors, the conclusions are as follows:

(*a*) too-fine meshes produced rather inaccurate calculations of the parameters;

(*b*) the interpolation of mesh-point velocity was relatively inaccurate in the neighbourhood of the cylinder, which did affect the subsequent calculations;

(*c*) as for the stream function, the accuracy was on the whole satisfactory, though as far as vorticity was concerned, finer meshes in some parts might have been more satisfactory;

(*d*) the calculations of pressure distribution caused somewhat problematical results in certain cases. This is because of the neglect of the unsteady terms in the original Navier–Stokes equations.

In connection with the computer system employed here, the authors are grateful to Assistant Professor T. Uemura of their laboratory for many instructive suggestions and discussions.

REFERENCES

APELT, C. J. 1958 The steady flow of a viscous fluid past a circular cylinder at Reynolds numbers 40 and 44. *Aero. Res. Counc. R. & M.* no. 3175.

BOUARD, R. & COUTANCEAU, M. 1980 The early stage of development of the wake behind an impulsively started cylinder for $40 < Re < 10^4$. *J. Fluid Mech.* **101**, 583.

COLLINS, W. M. & DENNIS, S. C. R. 1973 Flow past an impulsively started circular cylinder. *J. Fluid Mech.* **60**, 105.

COUTANCEAU, M. & BOUARD, R. 1977*a* Experimental determination of the main features of the viscous flow in the wake of a circular cylinder in uniform translations. Part 1. Steady flow. *J. Fluid Mech.* **79**, 231.

COUTANCEAU, M. & BOUARD, R. 1977*b* Experimental determination of the main features of the viscous flow in the wake of a circular cylinder in uniform translations. Part 2. Unsteady flow. *J. Fluid Mech.* **79**, 256.

HAMIELEC, A. E. & RAAL, J. D. 1969 Numerical studies of viscous flow around circular cylinders. *Phys. Fluids* **12**, 11.

HONJI, H. & TANEDA, S. 1969 Unsteady flow past a circular cylinder. *J. Phys. Soc. Japan* **27**, 1668.

PATEL, V. A. 1976 Time-dependent solutions of the viscous incompressible flow past a circular cylinder by the method of series truncation. *Comp. Fluids* **4**, 13.

SCHWABE, M. 1935 Über die Druckermittlung in der nichtstationären ebenen Strömung. *Ing. Arch.* **6**, 34.

SON, J. S. & HANRATTY, T. J. 1969 Numerical solutions for the flow around a cylinder at Reynolds numbers of 40, 100 and 500. *J. Fluid Mech.* **35**, 369.

TIMME, A. 1957 Über die Geschwindigkeitsverteilung in Wirbeln. *Ing. Arch.* **25**, 205.